machines

MDPI

Article

A Normalized Terzaghi Model and Time-Step FEA for Predicting the Adsorption of a Cylindrical Object in Subsea Salvage

Yibo Nan *, Feihong Yun *, Shaoming Yao, Ming Liu and Liquan Wang

College of Mechanical and Electrical Engineering, Harbin Engineering University, Harbin 150001, China
* Correspondence: nanyibo@hrbeu.edu.cn (Y.N.); yunfeihong@hrbeu.edu.cn (F.Y.); Tel.: +86-13045173896 (Y.N.); +86-15945683623 (F.Y.)

Abstract: This paper proposes a normalized Terzaghi model modified based on finite element analysis to predict the adsorption force of a cylindrical object for salvage from the seabed. The maximum relative error is less than 5% compared with finite element analysis. Furthermore, the time-step finite element method is adopted to analyze the effects of the lifting force and bury depth. With increased lifting force, the critical displacement is reduced slightly, soil separation on the bottom of the object occurs earlier, and the velocity increases more quickly at the same burial depth. In addition, the soil displacement on the bottom stops increasing earlier, and the off-mud process is completed earlier. With increased burial depth, soil separation takes considerably longer, velocity increases more slowly, the maximum soil displacement is increased, and the off-mud process takes longer to complete.

Keywords: adsorption; deep sea; rapid salvage; cylindrical objects

check for updates

Citation: Nan, Y.; Yun, F.; Yao, S.; Liu, M.; Wang, L. A Normalized Terzaghi Model and Time-Step FEA for Predicting the Adsorption of a Cylindrical Object in Subsea Salvage. *Machines* **2023**, *11*, 245. https://doi.org/10.3390/machines11020245

Academic Editor: Dan Zhang

Received: 9 December 2022
Revised: 26 January 2023
Accepted: 3 February 2023
Published: 7 February 2023

Copyright: © 2023 by the authors. Licensee MDPI, Basel, Switzerland. This article is an open access article distributed under the terms and conditions of the Creative Commons Attribution (CC BY) license (https://creativecommons.org/licenses/by/4.0/).

1. Introduction

With the increase in underwater activities, submersibles and aircraft often become submerged on the seabed because of high hydrostatic pressure in the deep sea, solar activity, high temperatures, and strong vibrations. Rapid salvage is required [1]. However, because of the interaction between the object and the subsea soil during rapid salvage operations, soil adsorption presents a significant challenge.

The salvage of deep-sea wrecks is one of the most difficult underwater operations. At sea depths below 200 m, ecosystems occupy more than 90% of the biosphere, connecting shallow and deep-sea ecosystems, playing a key role in nutrient regeneration, and providing harvestable fish resources [2]. Deep-sea salvage may lead to oil leaks from sunken ships, submersibles, and aircraft, which can cause pollution of the marine ecosystem. The consequence of severe pollution can be massive economic losses [3]. However, in the salvage process, extracting the object from the seabed mud is the first thing to be considered, and in this regard, the adsorption force of the soil is the key factor.

NCELI [4] tested a series of systematic and well-developed small-scale models in the laboratory in order to study the adsorption force. The results of the tests were used to classify salvage operations into long and short off-mud cases. Vesic [5] used anchor plate tests in soft clay to explain the mechanism of the adsorption force and derive a theoretical formula. The results showed that when the anchor plate moved upward under the lifting force, a difference in the pore water pressure above and below the anchor plate was produced, and this was the adsorption force. Ninomiya [6–8] analyzed the effects of bottom immersion time on the adsorption force. Das [9–11] investigated the variation between the damage coefficient of the adsorption and the burial depth using hollow anchors to increase the pore water pressure by venting air into the bottom of the flat anchors. Sawicki [12] proposed two stages, a "without-seam phase" and a "with-seam phase", for the lifting process in saturated clay. Zhou [13], on the basis of Sawicki, proposed a transition phase

between the without-seam and with-seam stages. Sui [14] used the finite element software ANSYS to simulate the adsorption force of the submerged structure and studied the relationship between the adsorption force, the depth of the mud, and the internal friction angle of the submerged structure. Hu [15] focused on the trifold lateral friction resistance model and its analytical solution under different loading states. Meyerhof [16] assumed that drainage conditions were the determining factor for the adsorption force and tested the magnitude of the adsorption force applied to the structure by experimentally loading it slowly over a period of time. Qiu [17] studied the effect of the water content on the adsorption force. Jin [18] divided the factors affecting adsorption force into three categories: the nature of the structure, the substrate in contact with the structure, and the immersion depth of the structure in the sediment. Referring to the traditional Terzaghi bearing capacity theory, the theoretical formula for the adsorption force of the sediment on the structure was calculated using the Skempton model. At present, the adsorption force formula is mainly used for submarine structures such as pile boots and caissons and is primarily developed from the foundation bearing capacity formula, which cannot be directly used to calculate the adsorption force. The earliest adsorption force formula was proposed by the U.S. Naval Civil Engineering Laboratory, which found that the salvage force was much greater than the self-weight of the structure in the submarine salvage and proposed an empirical formula based on the test results. However, this had limitations in that the coefficients in the empirical formula needed to be determined. Han [19] studied the relationship between lifting speed and adsorption force. Fang [20] carried out a study of adsorption forces through field tests of buoyancy variations using a model of a subsea bottom-supported foundation. Timir Karmakar [21] conducted an analytical study of the two-dimensional problem of lifting an object from the top of a fully saturated, rigid, porous bed. Davie and Sutherland [22] found in a series of experiments that structures subjected to upward force were easier to control, which reduced engineering accidents. Cong [23] analyzed the soil adsorption mechanism from a chemical point of view and also studied the factors affecting the adsorption, such as soil surface properties, surface characteristics, and the nature of the ions. Michalski [24,25] addressed the problem of calculating parameters for lifting objects of axisymmetric shape from the seabed and derived approximate algebraic formulas for lifting objects stranded on the seabed, proposing a parametric method suitable for assessing the suction of slender objects on the seabed and predicting the time of object release.

This paper proposes an improved Terzaghi model based on finite element analysis to predict the adsorption force of a cylindrical object to be salvaged from the seabed. The maximum relative error is less than 5% compared with finite element analysis. The effects of the lifting force and burial depth are further analyzed using time-step finite element analysis.

2. The Object and Salvage Process

When a fallen object is salvaged from the seabed, it is subjected to the adsorption force of the mud. The adsorption force is generally the interaction between the structure, the soil, and the liquid, which is usually water. The adsorption force consists of three elements: the adhesion between the soil and the bottom surface of the object's structure, the negative water pressure generated during the lifting of the structure, and the lateral frictional resistance generated between the soil and the side of the structure. When the lifting starts, the soil is deformed by the adsorption force and friction resistance. When the critical point of the adsorption force is reached, the soil on the bottom of the structure starts to separate from the structure surface; however, the soil on both sides of the structure has not been separated completely. Although the soil is separated from the structure's bottom, the soil on both sides is still lifted with the structure until a new equilibrium is reached again. As the lifting continues, the soil on both sides moves again and separates from the surface of the structure until the structure is fully lifted up and away from the mud. The movement of the fallen object and the soil is illustrated in Figure 1.

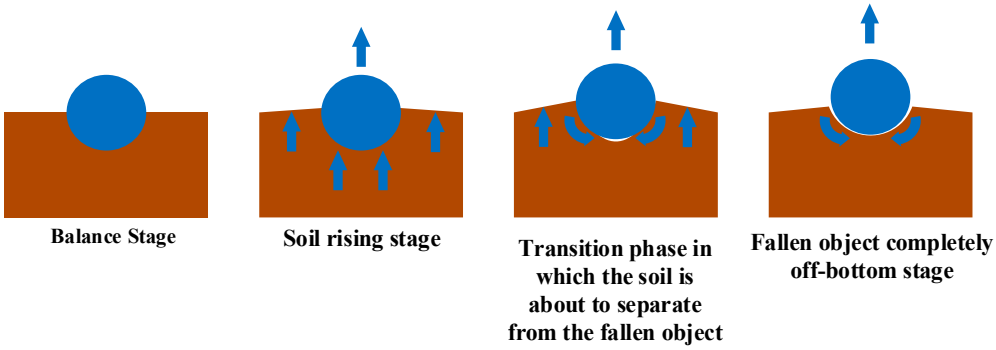


Figure 1. Schematic diagram of the fallen object and soil movement trend.

3. Results of Off-Mud Process Modeling and FEA

In this section, the off-mud model is created to analyze the behavior of the mud during the lifting. The simulation results are compared with the Terzaghi model, and the Terzaghi model is then modified to improve the model error.

3.1. Off-Mud Modelling

The Mohr–Coulomb model can be applied to loose or cemented granular materials that yield under shear stress, and the magnitude of the shear stress limit depends only on the maximum and minimum principal stresses. In addition, the Mohr–Coulomb model has two failure criteria: tensile and shear. The location of the stress point in the envelope is controlled by both the uncorrelated flow of the shear damage and the correlation law of the tensile damage.

3.1.1. Failure Criterion

In the principal stress space, the incremental expression of Hooke's law in terms of the generalized stress and stress increment is given by [26],

$$\begin{aligned} \Delta\sigma_1 &= \alpha_1\Delta\varepsilon_1^e + \alpha_2\left(\Delta\varepsilon_2^e + \Delta\varepsilon_3^e\right) \\ \Delta\sigma_2 &= \alpha_1\Delta\varepsilon_2^e + \alpha_2\left(\Delta\varepsilon_1^e + \Delta\varepsilon_3^e\right) \\ \Delta\sigma_3 &= \alpha_1\Delta\varepsilon_3^e + \alpha_2\left(\Delta\varepsilon_1^e + \Delta\varepsilon_2^e\right), \end{aligned} \tag{1}$$

In these equations, α_1 and α_2 are the material constants defined by the shear modulus and bulk modulus.

$$\begin{aligned} \alpha_1 &= K + \tfrac{4}{3}G \\ \alpha_2 &= K - \tfrac{2}{3}G, \end{aligned}$$

The combined Mohr–Coulomb criterion with the tensile failure is shown in Figure 2.

The failure envelope $f(\sigma_1, \sigma_3) = 0$ is defined by the shear failure criterion, $f^s = 0$, from A to B,

$$f^s = \sigma_1 - \sigma_3 N_\phi + 2c\sqrt{N_\phi}, \tag{2}$$

$$\text{and } N_\varphi = \frac{1+\sin\phi}{1-\sin\phi}.$$

This equation is defined by the tensile failure criterion, $f^t = 0$, from B to C,

$$f^t = \sigma_3 - \sigma^t, \tag{3}$$

where ϕ is the angle of the internal friction, c is the cohesive force, and σ_t is the tensile strength.

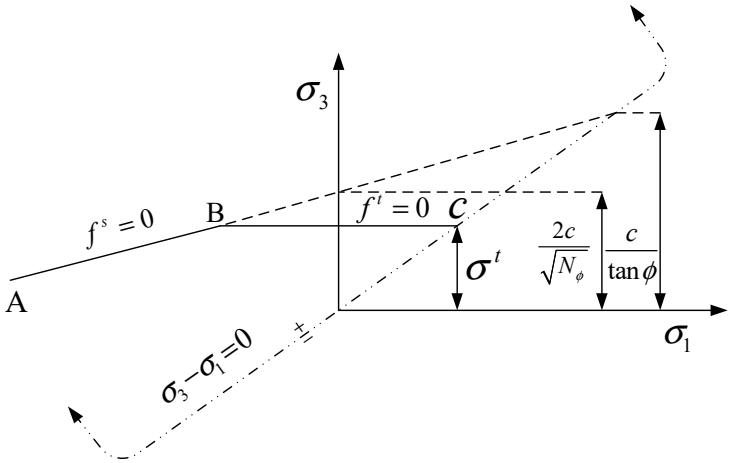


Figure 2. Mohr–Coulomb failure guidelines.

3.1.2. Mobility

Two functions, g^s and g^t, are used to represent the shear plastic flow and tensile plastic flow patterns. The function g^s corresponds to the uncorrelated flow [26].

$$g^s = \sigma_1 - \sigma_3 N_\psi \text{ and} \tag{4}$$

$$N_\psi = \frac{1 + \sin\psi}{1 - \sin\psi},$$

where ψ is the expansion angle.

The function g^t corresponds to the correlation law.

$$g^t = -\sigma_3. \tag{5}$$

Different laws are chosen by defining the region in which the stress point is located. As shown in Figure 3, this is the formula that defines the positive and negative domains:

$$h = \sigma_3 - \sigma^t + a^p(\sigma_1 - \sigma^p), \tag{6}$$

where a^p and σ^p are constants and,

$$a^p = \sqrt{1 + N_\varphi^2} + N_\varphi$$
$$\sigma^p = \sigma^t N_\varphi - 2c\sqrt{N_\varphi}$$

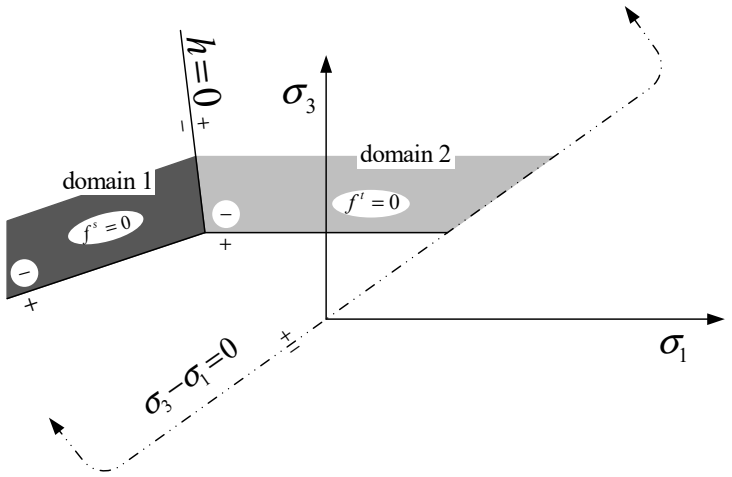


Figure 3. Definition domain of the laws of the Mohr–Coulomb model.

When the stress point falls within shear damage region 1 and the stress point conforms to the curve $f^s = 0$, the uncorrelated flow law derived from the function g^s is applicable. When the stress point falls within tensile damage region 2 and the stress point conforms to the curve $f^t = 0$, the correlation law derived from the function g^t is applicable.

3.1.3. Interface Model

The interface cells are assigned as a triangle, so that any node on an interface corresponds to an associated area. The area of any quadrilateral is defined by two triangular interface cells; nodes are located at the vertices of each interface cell, and interface nodes are formed when an interface cell connects to another mesh surface, as shown in Figure 4.

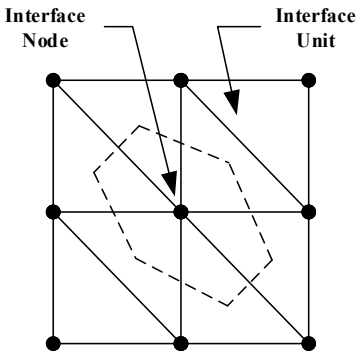


Figure 4. Interface node-related area distribution.

The interface can be treated as a "shrinkage band" that can be stretched and allows other surfaces to be connected to the interface with higher sensitivity when they pierce each other. The target surface, that is, the solid surface of the unit, can link the interface unit to the interface node. The normal stress at the interface is determined by the orientation of the target surface. The absolute normal impalement between the interface nodes and the target surface and the relative shear velocity are first derived at each time step of the calculation, and finally the tangential and normal force magnitudes are calculated using the interface intrinsic model. The expressions for the tangential and normal forces at the interface at the moment of $t + \Delta t$ when the interface is in the elastic phase are [27],

$$\begin{aligned} F_n^{(t+\Delta t)} &= k_n u_n A + \sigma_n A \\ F_{si}^{(t+\Delta t)} &= F_{si}^{(t)} + k_s \Delta u_{si}^{(t+0.5\Delta t)} A + \sigma_{si} A, \end{aligned} \tag{7}$$

where $F_n^{(t+\Delta t)}$ is the normal force vector at the time of $t + \Delta t$, $F_{si}^{(t+\Delta t)}$ is the tangential force at the time of $t + \Delta t$, u_n is the absolute displacement of the interface node penetration into the target surface, and Δu_{si} is the relative shear displacement increment vector. σ_n and σ_{si} are the additional normal and additional tangential stresses, both caused by the initialization of the interface stresses. k_s is the tangential stiffness of the interface unit, k_n is the normal stiffness of the interface unit, and A is the area represented by the interface nodes.

The model of the interface is shown in Figure 5. For the Coulomb sliding interface unit, there are two states of the mutual contact and relative sliding between the interface and the target surface, and according to the Coulomb shear strength criterion, the tangential force, F_{smax}, required for the relative sliding of the interface and the target surface, can be obtained as [27],

$$F_{\text{smax}} = c_{if} A + \tan \varphi_{if} (F_n - uA), \tag{8}$$

where c_{if} is the interface cohesion, φ_{if} is the interface friction angle, and u is the water pressure.

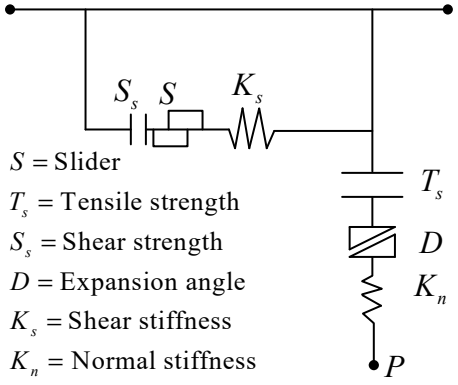


Figure 5. Schematic diagram of the interface unit principle.

When the tangential force on the interface is less than the maximum tangential force, namely, $|F_s| < F_{s\max}$, the interface is in the elastic stage. When the tangential force on the interface is equal to the maximum tangential force, that is, $|F_s| = F_{s\max}$, the interface is in the plastic stage.

When the magnitude of the tensile stress on the interface exceeds the tensile strength on the interface, the interface will be damaged, and the normal and tangential forces on the interface will become zero at the moment of interface damage. In general, the default tensile strength of the interface is zero.

The existence of interface nodes not only reflects the contact of the interface but also the transfer of the contact force. It is assumed that the stresses at the nodes are distributed over the representative areas of the nodes. Each node on the interface is associated with a parameter and can also have its own node with different parameters.

The normal and tangential stiffnesses of the interface are set at 10 times the equivalent stiffness of the "hardest" adjacent area [27],

$$k_n = k_s = 10\max\left(\frac{K + \frac{4G}{3}}{\Delta Z_{\min}}\right), \tag{9}$$

where K is the bulk modulus, G is the shear modulus, and $\Delta Z_{\min}$ is the minimum dimension over the connection area in the normal direction of the interface, as shown in Figure 6.

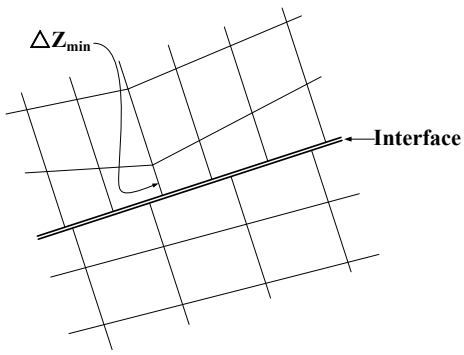


Figure 6. Schematic diagram of the minimum dimensions in the normal direction of the interface.

The interface parameters to be determined include cohesion c, friction angle φ, tangential stiffness k_s, and normal stiffness k_n. The parameters related to the interface of this model are listed in Table 1.

Table 1. Interface parameters.

Cohesion c (Pa)	Friction Angle φ (°)	Tangential Stiffness k_n (Pa)	Normal Stiffness k_s (Pa)
5.6×10^3	2.16	1×10^8	1×10^8

3.1.4. Soil Parameters

The soil density is 1.29 g/cm^3, and it is a silty soil. The Poisson's ratio of the silty soil is 0.3, and the elasticity modulus is 80,000 kN/m^2.

The bulk modulus K, shear modulus G, Young's modulus E, and Poisson's ratio v are related as [27],

$$K = \frac{E}{3(1-2v)}, \tag{10}$$

$$G = \frac{E}{2(1+v)}. \tag{11}$$

The parameters of the silty soil are listed in Table 2.

Table 2. The parameters of the silty soil.

Density (kg/m^3)	Bulk Modulus (Pa)	Shear Modulus (Pa)	Cohesion (kPa)	Friction Angle (°)	Tensile Strength (Pa)
1290	6.7×10^7	3.1×10^7	7.0	2.7	1×10^8

3.1.5. Object Parameters

The density of the object is 3002 kg/m^3, Poisson's ratio is 0.33, and the modulus of elasticity is 7.17×10^{10} Pa. The shear modulus is calculated as 2.70×10^{10} Pa, and the bulk modulus is 7.03×10^{10} Pa. The parameters of the object are listed in Table 3.

Table 3. Parameters of the object.

Density (kg/m^3)	Bulk Modulus (Pa)	Shear Modulus (Pa)	Diameter (m)	Length (Pa)
3002	7.03×10^{10}	2.70×10^{10}	2	14

3.2. Finite Element Analysis

The following assumptions are made for this simulation:

1. The deformation of the cylindrical structures is not considered;
2. The soil is saturated;
3. The particles of the soil are incompressible.

The parameters of the soil model are listed in Table 4. Because the soil close to the interface is affected by the lifting force, the soil and cylinder near the interface are refined.

Table 4. Simulation envelope of the soil.

Length (m)	Width (m)	Height (m)
14	12	6

Flow Chart of the Simulation

The silty soil and object model is shown in Figure 7.

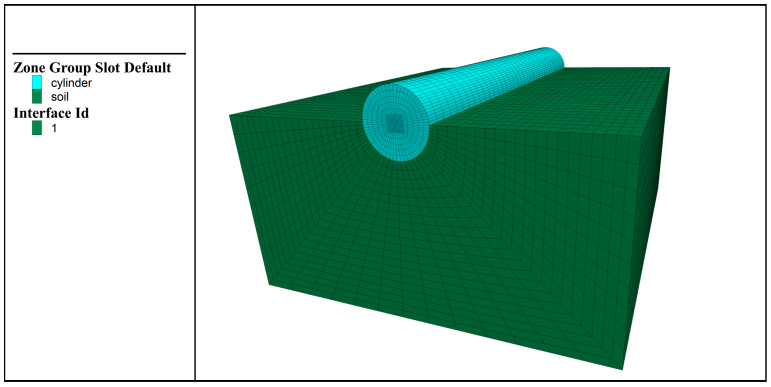


Figure 7. Silty soil and object model.

The simulation flowchart is shown in Figure 8.

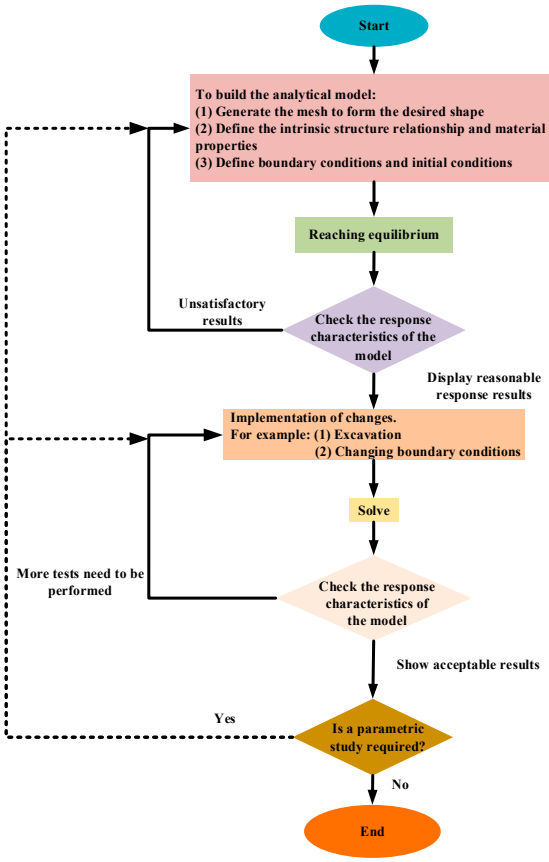


Figure 8. Flowchart of the simulated solution process.

3.3. Initial Stress and Off-Mud Process

The existence of initial ground stress and displacement affects the simulation results. Before the salvage, both need to be included in the simulation.

3.3.1. Initial Stress

In the analysis of the initial stress equilibrium of the silty soil, the criterion for the system to reach equilibrium is specified as the ratio of the maximum unbalanced force to 1×10^{-5}. In other words, when the ratio of the maximum unbalanced force to the average of the initially applied nodal force is no more than 1×10^{-5}, the maximum unbalanced force is negligible, and the system is in convergent equilibrium. In this case, the model of the object with a depth of 1.6 m is used.

In Figure 9, it can be seen that the maximum unbalanced force ratio gradually tends to zero as the time steps increase, until finally the system reaches equilibrium under gravity. However, it is necessary to observe the changes in velocity and displacement in the model to ensure they converge to constants so as to further verify that the system has reached true equilibrium. The node at the bottom of the object was selected, and the time-step curves of its velocity and displacement in the z-direction were plotted, as shown in Figures 10 and 11. It can be seen that as the time step increases, the velocity of the node at the bottom approaches zero and the displacement gradually approaches a constant, which shows that the system has reached true equilibrium.

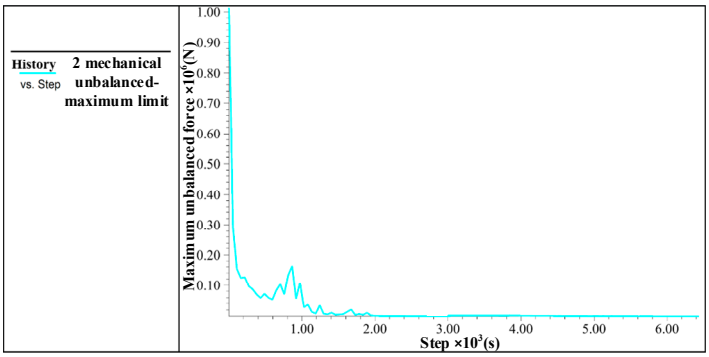


Figure 9. Maximum unbalanced force.

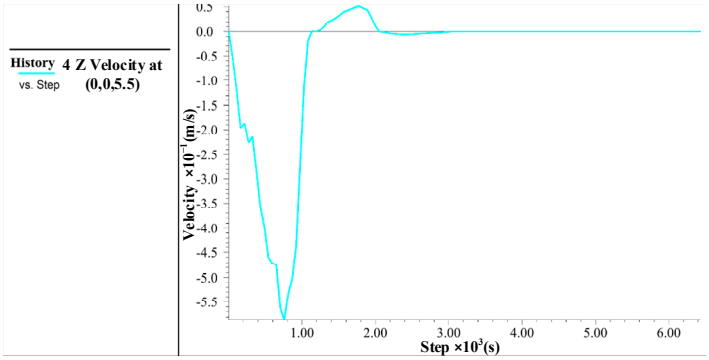


Figure 10. Nodal velocity at the bottom of the object.

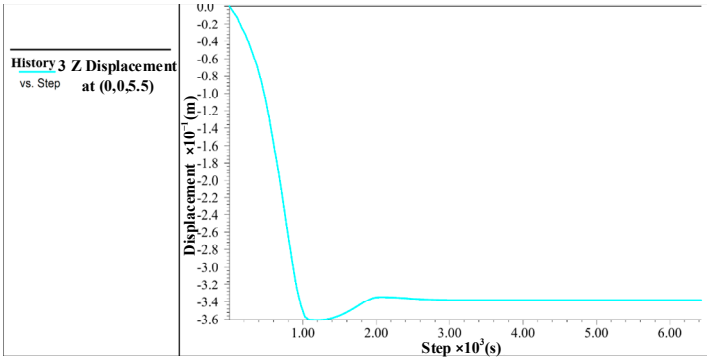


Figure 11. Node displacement at the bottom of the object.

The initial stress of the system is shown in Figure 12. When the model reaches true equilibrium, the stress of the soil is consistent with the real situation.

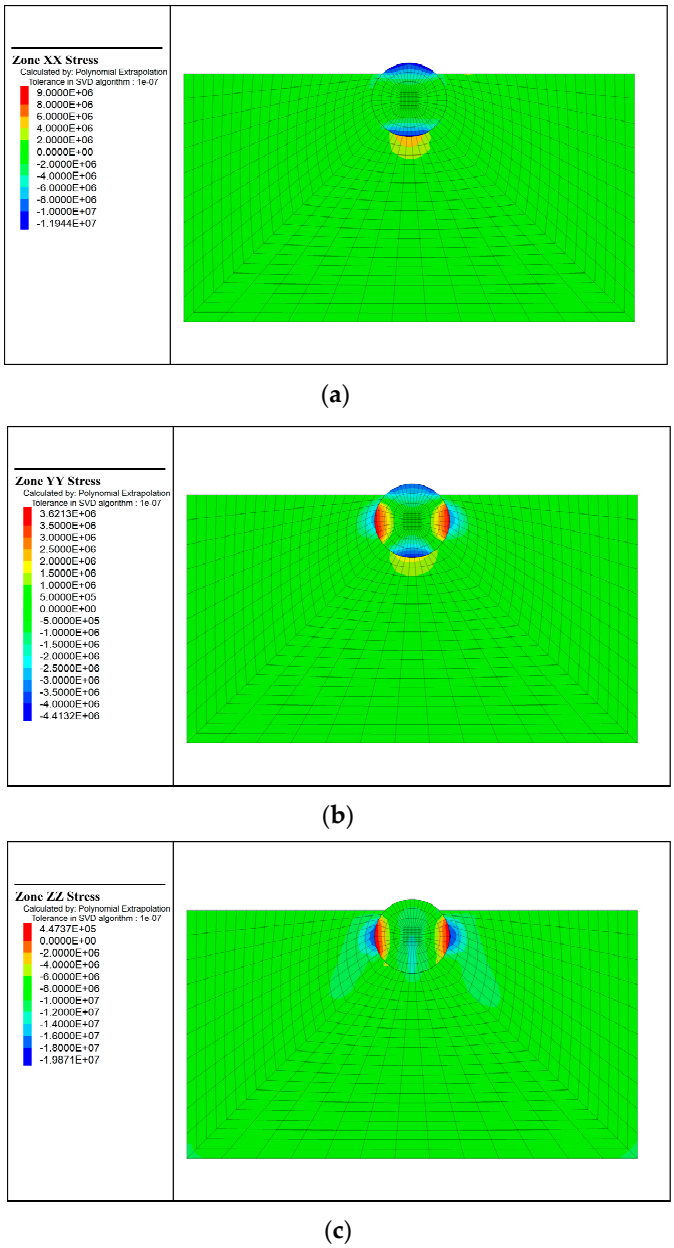


Figure 12. Initial stress field: (**a**) x-directional stress in the initial equilibrium; (**b**) y-directional stress in the initial equilibrium; and (**c**) z-directional stress in the initial equilibrium.

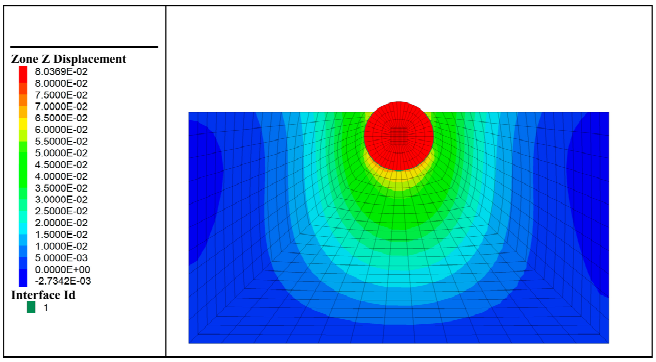
The x- and y-directional stresses are nearly constant in most of the area, and the stress concentration occurs only on the top, bottom, and both sides of the object, as shown in Figure 12a,b. This is due to the gravity-produced displacement of the object in the negative direction of the *z*-axis and the lateral displacement of the soil close to the object under the effect of hydrostatic pressure. From the z-direction stress, it can be seen in Figure 12c that the stress concentration appears on both sides of the object. The reason for this is that the solid structure on top of the object is compressed by the weight of the soil on both sides. At this moment, the maximum compressive stress is 19.8 MPa.

3.3.2. Off-Mud Simulation

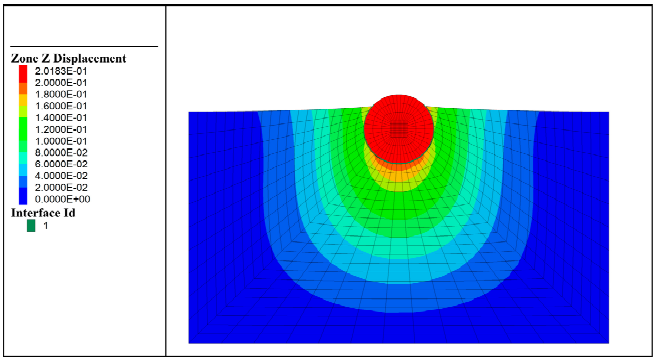
To investigate the effect of the depth in the mud, the salvage process can be divided into two stages. The first stage is from when the object starts to move upward until it is fully out of the mud; the second stage is from when the object is fully out of the mud until it is out of the water. Because this paper focuses on the salvage of the object from

the mud, the x- and y-directional displacements are horizontal displacements, which have little influence on the salvage process; therefore, only the z-directional displacement of the object is discussed.

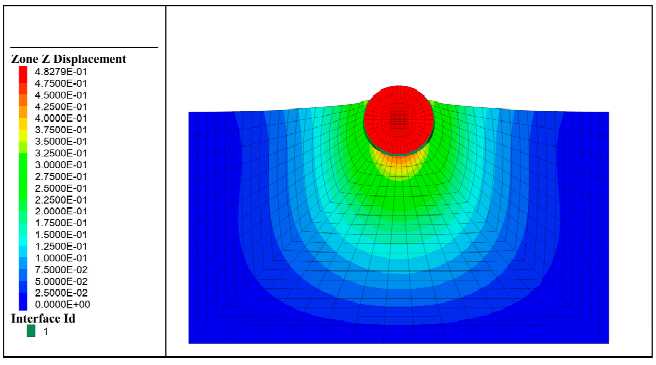
The simulation of the object moving out of the mud is shown in Figure 13. The object starts to move up, but the bottom of the object does not separate from the soil (no gap) because of the adsorption force of the silty soil under the action of the upward lifting force, as shown in Figure 13a. As shown in Figure 13b, the soil at the bottom is subjected to an upward tensile strain, and the tensile strain in the middle of the soil gradually increases, and the soil at the bottom is about to be separated. Figure 13c shows that as the upward tensile strain continues to increase, the soil close to the bottom of the object starts to separate from the object because of gravity, and a gap is produced. With an increase in the tensile strain, the gap extends until the mud is separated from the object. As illustrated in Figure 13d, it can be seen that at the beginning, the displacements of the object and the bottom soil are equal to each other. As the time increases, the bottom soil displacement becomes less than that of the object, and the gap is produced; this difference increases with time until the displacement of the mud stops increasing and the object is fully out of the mud.



(**a**)

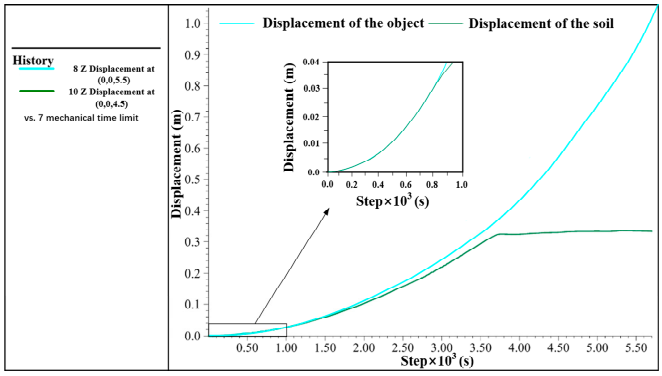


(**b**)



(**c**)

Figure 13. *Cont.*



(**d**)

Figure 13. Initial stress field: (**a**) without gap phase; (**b**) transition phase; (**c**) with gap phase; and (**d**) the displacement curves of the object and bottom soil.

4. Comparison and Modification of the Terzaghi Model

The Terzaghi model [28] can be used to describe the lifting force,

$$F_t = 5A\tau_f\left(1 + 0.2\frac{de^{\sqrt{d}}}{B}\right)\left(1 + 0.2\frac{B}{L}\right)\sin\left(\frac{\pi A_R}{2A_P}\right), \quad (12)$$

where A is the horizontal projection area of the structure, τ_f is the shear strength of the soil, and , B, and L are the burial depth, width, and length of the structure, respectively; A_R is the contact area of the structure immersed in the soil and A_P is the total surface area of the structure.

4.1. Comparison with FEA Results

The Terzaghi model results were compared with the simulation results to verify the model errors, as shown in Figure 14. The trend of the Terzaghi results is consistent with the FEA results but slightly higher.

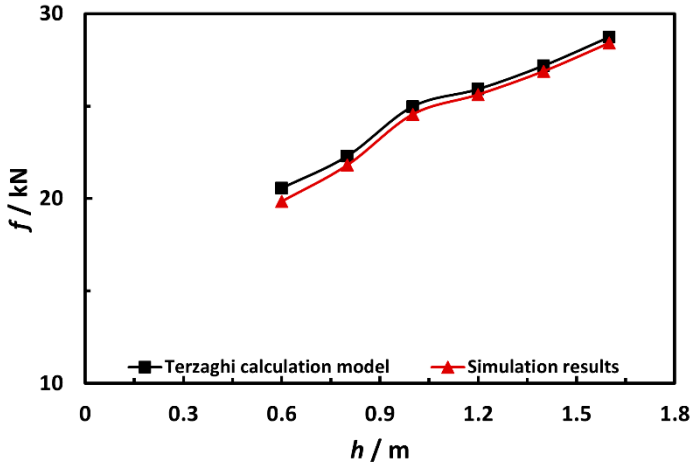


Figure 14. Validation of simulation results.

4.2. Normalized Terzaghi Model and Modification

The relative error of the Terzaghi model and its comparison with the FEA results are plotted in Figure 15. The maximum relative error is 3.51%.

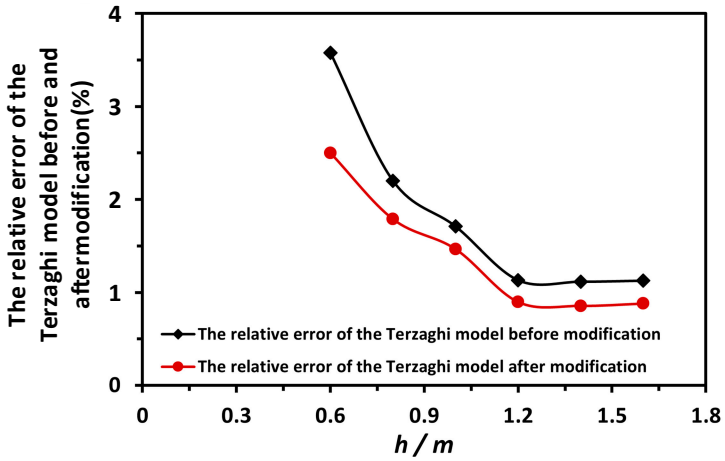


Figure 15. The relative error of the Terzaghi model before and after modification.

To improve the prediction errors, a normalized Terzaghi model is proposed, as set out below.

Define the nondimensional burial depth β, the nondimensional width γ, and the nondimensional burial surface λ, as:

$$\begin{aligned} \beta &= \tfrac{d}{B} \\ \gamma &= \tfrac{B}{L} \\ \lambda &= \tfrac{A_R}{A_P}. \end{aligned} \tag{13}$$

The modification coefficient ψ, is defined as:

$$\psi = a(1 + b\beta). \tag{14}$$

Equation (12) can be rewritten as,

$$\begin{aligned} F_t{}' &= \psi F_t \\ &= 5A\tau_f a(1 + b\beta)\left(1 + 0.2e^{\sqrt{B}}\beta e^{\sqrt{\beta}}\right)\left(1 + 0.2\tfrac{B}{L}\right)\sin\left(\tfrac{\pi A_R}{2A_P}\right) \\ &= 5A\tau_f a(1 + b\beta)\left(1 + 3.838\beta e^{\sqrt{\beta}}\right)(1 + 0.2\gamma)\sin\left(\lambda\tfrac{\pi}{2}\right). \end{aligned} \tag{15}$$

where a = 0.934 and b = 0.165.

The relative error of the normalized Terzaghi model after modification is plotted in Figure 15, and the maximum relative error after modification is 2.49%.

5. Time-Step Analysis

The static adsorption force can be accurately predicted using the improved Terzaghi model. When the speed is not sufficiently low, the Terzaghi model is less effective for adsorption force prediction. In this situation, the time-step simulation can be used.

5.1. Effects of Lifting Force and Burial Depth on Critical Displacement

The critical displacement is the displacement that occurs when bottom separation occurs. As shown in Figure 16, a depth of 1.6 m and a lifting force of 50 t were used as reference parameters for the analysis, and these were selected according to a recent project requirement.

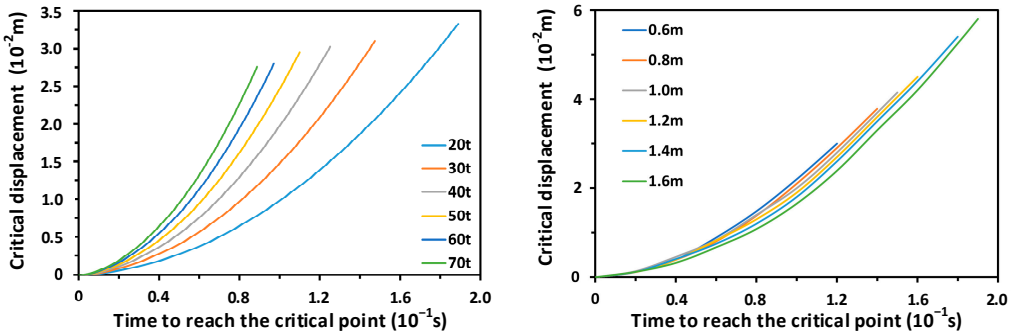


Figure 16. Effects of lifting force and burial depth on the critical displacement of the object before separation: (**a**) burial depth, 1.6 m; (**b**) lifting force, 50 t.

As shown in Figure 16a, the displacement of the object and the soil increases in a nonlinear way with lifting forces of 20 t, 30 t, 40 t, 50 t, 60 t, and 70 t. With increased lifting force, the critical displacement reduces slightly but does not linearly decrease. With a large lifting force and at the same burial depth, the separation occurs earlier. As shown in Figure 16b, an increase in burial depth with the same lifting force considerably increases the time taken for separation to occur.

5.2. Effects of Lifting Force and Burial Depth on Displacement

The displacements with different lifting forces are plotted in Figure 17a. With a large lifting force and the same burial depth, the displacement increases more quickly. Displacements with different burial depths are plotted in Figure 17b. The displacement increases more quickly when the burial depth is smaller, and vice versa.

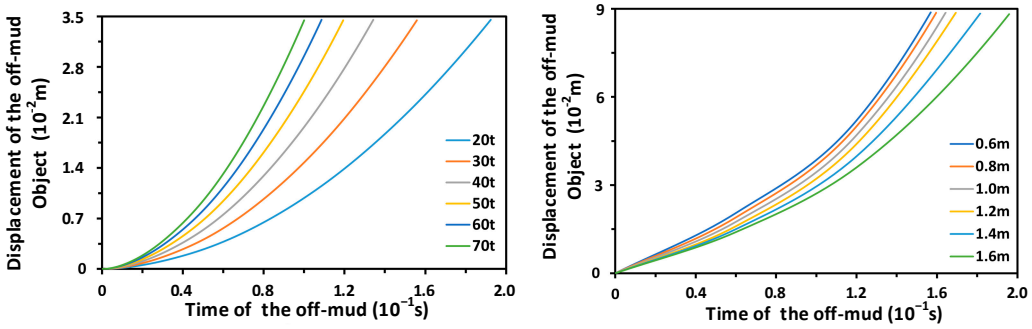


Figure 17. Displacement with different lifting forces and burial depths: (**a**) burial depth, 1.6 m; (**b**) lifting force, 50 t.

5.3. Effects of Lifting Force and Burial Depth on Velocity

The velocity in the lifting process is plotted in Figure 18a, with lifting forces ranging from 20 t to 70 t. The velocity increases with time as the constant lifting forces are applied. With a large lifting force, the velocity increases much more quickly. The displacements with different burial depths and the same lifting force of 50 t are plotted in Figure 18b. The displacement increases with time. At a large burial depth, the velocity increases more slowly.

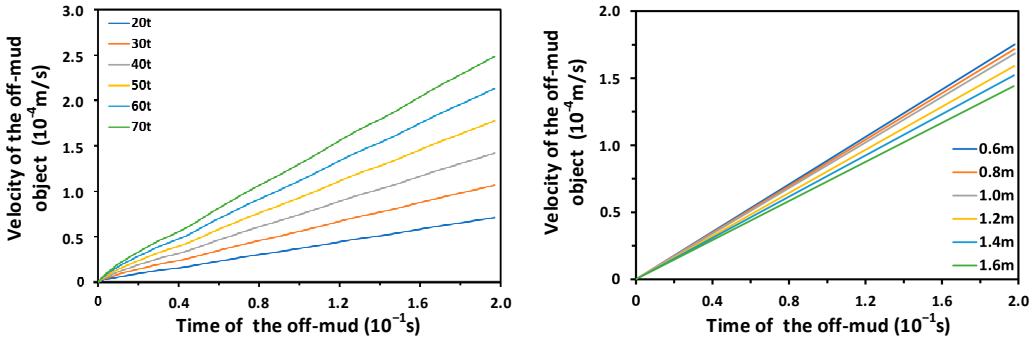


Figure 18. Effects of lifting force and burial depth on velocity: (**a**) burial depth, 1.6 m; (**b**) lifting force, 50 t.

5.4. Effects of Lifting Force and Burial Depth on Soil Displacement

Bottom soil displacement increases when the object is lifted until it is fully separated from the soil and the off-mud process is complete.

Soil displacements with different lifting forces are plotted in Figure 19a. With a big lifting force and the same burial depth, the soil displacement stops increasing sooner, and the off-mud process is also completed earlier. When the burial depth is increased with the same lifting force, the maximum soil displacement increases. When the burial depth is decreased with the same lifting force, the displacement stops increasing slightly earlier, as shown in Figure 19b.

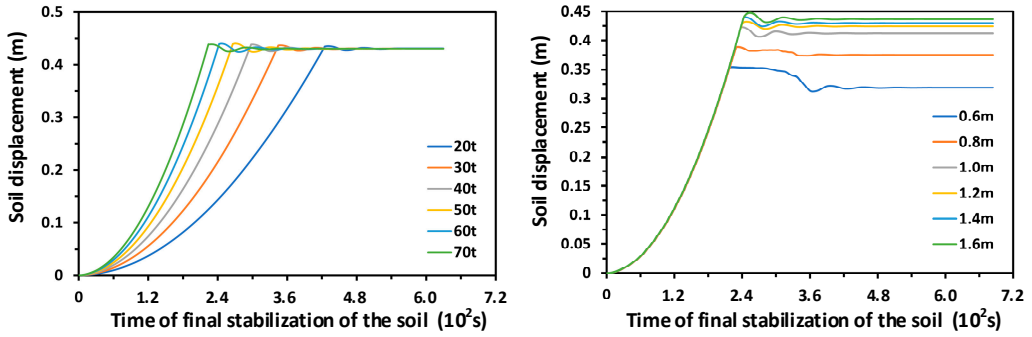


Figure 19. Displacement of the soil at the bottom with different lifting forces and burial depths: (**a**) burial depth, 1.6 m; (**b**) lifting force, 50 t.

6. Conclusions

This paper proposes a normalized Terzaghi model that has been modified according to finite element analysis to predict the adsorption force of a cylindrical object for salvage from the seabed. The effects of the lifting force and burial depth are also analyzed using time-step finite element analysis. The following conclusions can be drawn:

1. The normalized Terzaghi model can be used to predict the adsorption force in the salvage of cylindrical objects. The maximum relative error is less than 2.49% compared with finite element analysis;
2. Time-step finite element analysis can be used to investigate the off-mud process with regard to the effects of the lifting force and burial depth;
3. With increased lifting force and the same burial depth, the critical displacement is reduced slightly, soil separation on the bottom of the object occurs earlier, the velocity increases more quickly, soil displacement on the bottom stops increases earlier, and the off-mud process is completed earlier;

4. With increased burial depth, the time required for soil separation is considerably increased, the velocity increases more slowly, the maximum soil displacement is increased, and the off-mud process takes longer.

The above-mentioned normalized Terzaghi model is only suitable for long cylindrical objects and cannot be used for objects with rectangular or triangular cross sections or for objects with section dimensions equal to their length, where the end effects are dominant.

In future research, the normalized Terzaghi model could be further improved with regard to the effects of the lifting velocity and force, and the model could be verified using time-step finite element analysis as well as experiments.

Equation Symbols List

σ_1,σ_2,σ_3	The three components of the generalized stress vector.
α_1	The material constants defined by the shear modulus and bulk modulus.
α_2	The material constants defined by the shear modulus and bulk modulus.
ε_1,ε_2,ε_3	The principal strains.
N_φ	The internal friction angle coefficient.
ϕ	The angle of the internal friction.
c	The cohesive force.
σ_t	The tensile strength.
N_ψ	The expansion angle coefficient.
ψ	The expansion angle.
$F_n^{(t+\Delta t)}$	The normal force vector at the time of $t + \Delta t$.
$F_{si}^{(t+\Delta t)}$	The tangential force at the time of $t + \Delta t$.
u_n	The absolute displacement of the interface node penetration into the target surface.
Δu_{si}	The relative shear displacement increment vector.
σ_n	The additional normal stress.
σ_{si}	The additional tangential stress.
k_s	The tangential stiffness of the interface unit.
k_n	The normal stiffness of the interface unit.
A	The area represented by the interface nodes.
$F_{s\max}$	The tangential force.
c_{if}	The interface cohesion.
φ_{if}	The interface friction angle.
u	The water pressure.
K	The bulk modulus.
G	The shear modulus.
$\Delta Z_{\min}$	The minimum dimension over the connection area in the normal direction of the interface.
k_s	The tangential stiffness.
k_n	The normal stiffness.
E	Young's modulus.
v	Poisson's ratio.
A	The horizontal projection area of the structure.
τ_f	The shear strength of the soil.
d	The burial depth.
B	The width of the structure.
L	The length of the structure.
A_R	The contact area of the structure immersed in the soil.
A_P	The total surface area of the structure.
β	The nondimensional burial depth.
γ	The nondimensional width.
λ	The nondimensional burial surface.
ψ	The modification coefficient.

Author Contributions: Conceptualization, F.Y. and Y.N.; methodology, Y.N.; writing—original draft preparation, Y.N. and F.Y.; writing—review and editing, S.Y., L.W. and M.L.; validation, L.W. and S.Y.;

supervision L.W.; funding acquisition, F.Y. All authors have read and agreed to the published version of the manuscript.

Funding: This research was funded by the Heilongjiang Provincial Natural Science Foundation of China (LH2021E046); Key R&D Program of Shandong Province (2021JMRH0302).

Institutional Review Board Statement: Not applicable.

Informed Consent Statement: Not applicable.

Data Availability Statement: Not applicable.

Acknowledgments: The authors gratefully acknowledge the financial support from the Heilongjiang Provincial Natural Science Foundation of China (LH2021*E046); Key R&D Program of Shandong Province (2021JMRH0302).

Conflicts of Interest: All the authors have read and approved this version of the article, and due care has been taken to ensure the integrity of the work. The authors have no conflict of interests to declare.

References

1. Yan, Y.; Jin, H.; Zhang, Y.; Wang, J.; Guo, J. Statistical analysis of typical ship accidents in past 4 years and review of salvage equipment in China. In Proceedings of the 2019 5th International Conference on Transportation Information and Safety (ICTIS), Liverpool, UK, 14–17 July 2019. [CrossRef]
2. Drazen, J.C.; Smith, C.R.; Gjerde, K.M.; Haddock, S.H.D.; Carter, G.S.; Choy, C.A.; Clark, M.R.; Dutrieux, P.; Goetze, E.; Hauton, C.; et al. Opinion: Midwater ecosystems must be considered when evaluating environmental risks of deep-sea mining. *Proc. Natl. Acad. Sci. USA* **2020**, *117*, 17455–17460. [CrossRef] [PubMed]
3. Lee, M.; Jung, J.Y.; Park, K.C.; Choi, S.H. Environmental and economic loss analyses of the oil discharge from shipwreck for salvage planning. *Mar. Pollut. Bull.* **2022**, *155*, 111142. [CrossRef] [PubMed]
4. Lee, H. Breakout of partially embedded objects from cohesive seafloor soils. In Proceedings of the Offshore Technology Conference, Houston, TX, USA, 29 April 1973. [CrossRef]
5. Vesic, A.S. Breakout resistance of objects embedded in ocean bottom. *J. Soil. Mech. Found. Div.* **1971**, *97*, 1183–1205. [CrossRef]
6. Ninomiya, K.; Tagaya, K.; Murase, Y. A study on suction breaker and scouring of a submersible offshore structure. In Proceedings of the The Third Annual Offshore Technology Conference, Houston, TX, USA, 18 April 1971; pp. 297–304. [CrossRef]
7. Ninomiya, K.; Tagaya, K.; Murase, Y. A study on suction breaker and scouring of sit-on-bottom type offshore structure. In Proceedings of the The Fourth Annual Offshore Technology Conference, Houston, TX, USA, 30 April 1972; pp. 869–874. [CrossRef]
8. Ninomiya, K.; Tagaya, K.; Murase, Y. A study on suction breaker and scouring of bottom-sitting offshore. *J. Petrol. Technol.* **1973**, *25*, 279–287. [CrossRef]
9. Das, B.M. Model tests for uplift capacity of foundations in clay. *Soil. Found.* **1978**, *18*, 17–24. [CrossRef] [PubMed]
10. Das, B.M.; Shin, E.C.; Dass, R.N. Suction force below plate anchors in soft clay. *Mar. Georesour. Geotec.* **1994**, *12*, 71–81. [CrossRef]
11. Das, B.M. Behavior of a shallow plate anchor in clay under sustained loading. *Mar. Georesour. Geotec.* **1995**, *13*, 417–428. [CrossRef]
12. Sawicki, A.; Mierczynski, J. Mechanics of the breakout phenomenon. *Comput. Geotech.* **2003**, *30*, 231–243. [CrossRef]
13. Zhou, X.; Chow, Y.; Leung, C. Numerical modeling of break out process of objects lying on the seabed surface. *Comput. Geotech.* **2008**, *35*, 686–702. [CrossRef]
14. Sui, J. Study on Adsorption Power of Submersible Structure from Sediment. Master's Thesis, Dalian University of Technology, Dalian, China, 2009.
15. Hu, Y. Analysis of the Mechanism of Excavation Resistance of Special Shape Falling Object. Master's Thesis, Harbin Engineering University, Harbin, China, 2018.
16. Meyerhof, S. *Engineering Properties of Nuclear Technical, Report NO.3-699, Report 2*; U.S. Army Engineer Water Ways Experiment Station: Vicksburg, MI, USA, 1965.
17. Qiu, C.; Zhang, Q.; Yan, P.; Ji, Y. Experimental study of adhesion of clay. *Rock Soil Mech.* **2017**, *5*, 67–72. [CrossRef]
18. Jin, G.; Jin, T.; Chen, X.; Zhang, Z.; Luo, D. Experimental Research on Breakout Force of Embeded Objects from Sediments. *J. Nav. Acad. Eng.* **1998**, *3*, 49–53.
19. Han, L.; Jiang, M.; Zhang, R. Experiment Simulation of Absorption Force of Marine Structure Caisson. *Port. Eng. Technol.* **2009**, *46*, 43–45.
20. Fang, T.; Liu, G.; Ye, G.; Pan, S.; Shi, H.X.; Zhang, L. Field Test on Buoyancy Variation of a Subsea Bottom-Supported Foundation Model. *J. Mar. Sci. Eng.* **2019**, *7*, 143. [CrossRef]
21. Karmakar, T.; Sekhar, G.P. Lifting a large object from an anisotropic porous bed. *Phys. Fluids* **2016**, *28*, 093601. [CrossRef]
22. Davie, J.; Sutherland, H. Uplift resistance of cohesive soils. *J. Geotech. Eng. Div.* **1977**, *103*, 935–952. [CrossRef]
23. Cong, X.; Ren, L.; Chen, B. Study on Soil Adhesion Phenomenaby Chemical Adsorption. *Trans. Chin. Soc. Agric. Eng.* **1996**, *12*, 40–44.
24. Michalski, J. Parametric Method Applicable in Calculating Breakout Force and Time for Lifting Axisymmetric Objects from Seabed. *Pol. Marit. Res.* **2019**, *26*, 147–152. [CrossRef]

25. Michalski, J. Parametric Method Applicable in Assessing Breakout Force and Time for Lifting Slender Bodies from Seabed. *Pol. Marit. Res.* **2020**, *27*, 69–75. [CrossRef]
26. FLAC3D Base Commands. Available online: http://docs.itascacg.com/flac3d700/flac3d/docproject/source/flac3dhome.html (accessed on 20 January 2023).
27. Chen, Y.; Xu, D. *FLAC/FLAC3D Basic and Engineering Examples*, 2nd ed.; China Water and Power Press: Beijing, China, 2013; pp. 143–146.
28. Ma, J.; Yang, G.; Li, T. Study on Breakout Force of Embedded Objects from Seabed. *China Offshore Platf.* **2007**, *2*, 16–19.

Disclaimer/Publisher's Note: The statements, opinions and data contained in all publications are solely those of the individual author(s) and contributor(s) and not of MDPI and/or the editor(s). MDPI and/or the editor(s) disclaim responsibility for any injury to people or property resulting from any ideas, methods, instructions or products referred to in the content.